

This item is the archived peer-reviewed author-version of:

Evaluation of [^{18}F]BR420 and [^{18}F]BR351 as radiotracers for MMP-9 imaging in colorectal cancer

Reference:

Vázquez Naiara, Missault Stephan, Vangestel Christel, Deleye Steven, Thomae David, van der Veken Pieter, Augustyns Koen, Staelens Steven, Dedeurw aerdere Stefanie, Wyffels Leonie.- Evaluation of [^{18}F]BR420 and [^{18}F]BR351 as radiotracers for MMP-9 imaging in colorectal cancer
Journal of Labelled Compounds and Radiopharmaceuticals - ISSN 0362-4803 - 60:1(2017), p. 69-79

Full text (Publisher's DOI): <https://doi.org/doi:10.1002/JLCR.3476>

To cite this reference: <http://hdl.handle.net/10067/1390540151162165141>

1 **Evaluation of [¹⁸F]BR420 and [¹⁸F]BR351 as radiotracers for MMP-9 imaging in**
2 **colorectal cancer**

3 Abbreviated title: Evaluation of ¹⁸F-labeled MMP-9 radiotracers in a colorectal cancer model

4 Authors: Naiara Vazquez^{1,2,3}, Stephan Missault¹, Christel Vangestel^{2,4}, Steven Deleye², David
5 Thomae^{2,3}, Pieter Van der Veken³, Koen Augustyns³, Steven Staelens², Stefanie
6 Dedeurwaerdere¹, Leonie wyffels^{2,4}

7 ¹*Department of Translational Neurosciences, University of Antwerp, Antwerp, Belgium*

8 ²*Molecular Imaging Center Antwerp, University of Antwerp, Antwerp, Belgium*

9 ³*Laboratory of Medicinal Chemistry, University of Antwerp, Antwerp, Belgium*

10 ⁴*University Hospital Antwerp, Department of Nuclear Medicine, Edegem, Belgium*

11

12 Corresponding author:

13 Prof. dr. Leonie wyffels

14 University Hospital Antwerp

15 Department of Nuclear Medicine

16 Wilrijkstraat 10

17 2650 Antwerp, Belgium

18 Tel. +32 3 821 56 99

19 Leonie.wyffels@uza.be

20

21 Key words: MMP-9, PET, Colo205

22

23 **Abstract:**

24 Introduction: MMP-9 is a zinc dependent endopeptidase which is involved in the proteolytic
25 degradation of the extracellular matrix and plays an important role in cancer migration,
26 invasion and metastasis. The aim of this study was to evaluate the potential of MMP-tracers
27 [¹⁸F]BR420 and [¹⁸F]BR351 for MMP-9 imaging in a colorectal cancer xenograft model.

28 Methods: [¹⁸F]BR420 and [¹⁸F]BR351 were synthesized using an automated synthesis
29 module. For [¹⁸F]BR420 a novel and improved radiosynthesis was developed. Plasma
30 stability and MMP-9 targeting capacity of both radiotracers was compared in the Colo205
31 colorectal cancer model. MMP-9 and MMP-2 expression in the tumors was evaluated by
32 immunohistochemistry and in situ zymography.

33 Results: μ PET imaging as well as *ex vivo* biodistribution revealed a higher tumor uptake for
34 [¹⁸F]BR420 ($3.15 \pm 0.03\%ID/g$ versus $0.94 \pm 0.18\%ID/g$ for [¹⁸F]BR351 at 2 h p.i.) but
35 slower blood clearance compared to [¹⁸F]BR351. [¹⁸F]BR351 was quickly metabolized in
36 plasma with $20.28 \pm 5.41\%$ of intact tracer remaining at 15 min p.i. [¹⁸F]BR420 on the other
37 hand displayed a higher metabolic stability with $>86\%$ intact tracer remaining at 2 h p.i.
38 Immunohistochemistry revealed presence of MMP-9 and MMP-2 in the tumor tissue, which
39 was confirmed by *in situ* zymography. However, autoradiography analysis of tracer
40 distribution in the tumors did not correlate with MMP-9 expression.

41 Conclusion: [¹⁸F]BR420 displayed a higher tumor uptake and higher stability compared to
42 [¹⁸F]BR351, yet a low tumor-to-blood ratio and discrepancy between tracer distribution and
43 MMP-9 immunohistochemistry. Therefore both tracers will not be usefulness for MMP-9
44 imaging in colorectal cancer.

45

46 **1. Introduction**

47 Matrix metalloproteinases (MMPs) comprise a large family of several structurally related
48 zinc-dependent endopeptidases which contribute to the extracellular matrix (ECM)
49 proteolysis.^{1,2} All MMP family members present a common domain structure composed of at
50 least a predomain, a catalytic domain and a highly conserved active site domain.^{3,4} The
51 catalytic core-domain contains the active, protein-degrading ability of the proteinase, which
52 includes a metal binding site for Zn²⁺. The predomain acts as an internal inhibitor of MMP
53 activity, and activation occurs with cleavage of the predomain leading to a conformational
54 change to the active site. MMPs are synthesized as secreted or membrane-associated (MT-
55 MMPs) inactive zymogens, and must be proteolytically processed to an active state. This
56 processing involves removal of a cysteine residue that interacts with zinc ions from the active
57 site, thereby resulting in MMP activation. Based on their structure and substructure
58 specificity, human MMPs are divided into five groups: collagenases, gelatinases,
59 stromelysins, membrane-type metalloproteinases and the others.⁵

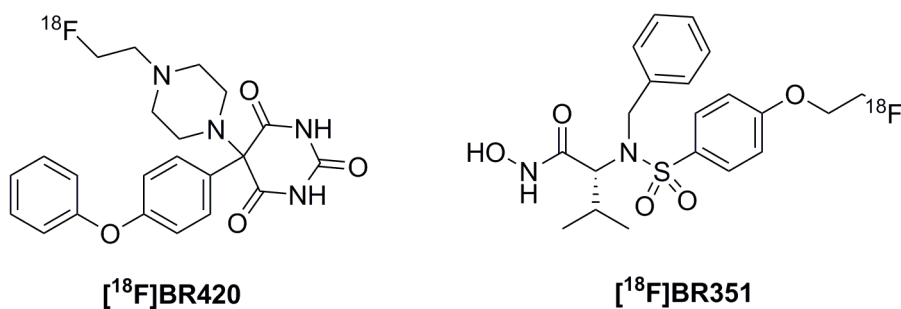
60 Because of their capacity to degrade the ECM, MMPs are known to play an important role in
61 several diseases.^{6,7,8,9} In particular in cancer, excess matrix degradation is one of the hallmarks
62 and an important component in the process of tumor progression.¹⁰ Among the large number
63 of MMPs, gelatinases A (MMP-2) and gelatinases B (MMP-9) are the most frequently
64 investigated proteases for their involvement in cancer migration, invasion and metastasis.^{11,12}
65 Particularly, MMP-9 can show both anti-cancer and tumor-promoting effects. A disturbance
66 of MMP-9 function in animals has been correlated with a decrease in tumor progression while
67 on the other hand overexpression of MMP-9 would induce angiogenesis and increase
68 malignant transformation.^{13,14} Colorectal cancer is the third most common cancer worldwide
69 and the forth most common cause of death.^{15,16} Considerable evidence has implicated MMPs
70 in established colorectal cancer, showing either an increased MMP expression or increased
71 MMP activity in this type of tumor. Overexpression of MMP-9 has been demonstrated in
72 human colorectal cancers, where the degree of overexpression has been shown to correlate
73 with stage of disease and/or prognosis.¹⁷

74 Due to their role in cancer, MMPs have gained significant attention as therapeutic target. The
75 search for MMP inhibitors has been largely carried out during the last decades.^{18,19} There are
76 several requirements for the design of an appropriate MMP inhibitor: the presence of a
77 functional group providing a hydrogen bond with the enzyme, side chains able to interact with

78 the enzyme sub sites and a zinc binding group. The development of MMP inhibitors with a
79 high selectivity towards a particular MMP however remains a big challenge. Most inhibitors
80 are broad spectrum MMP inhibitors although some display favourable binding affinity for a
81 specific MMP type. Recently, a barbiturate-based fluorescent MMP inhibitor (Cy5.5-AF443)
82 with a high affinity toward MMP-2 and MMP-9 has been successfully used for the *in vivo*
83 evaluation of MMP-2/-9 expression in mouse models of colorectal cancer.^{20, 21} The use of the
84 fluorescent label however requires the application of invasive endoscopic techniques for
85 imaging of MMP activity in the colon. Targeting MMP with Positron Emission Tomography
86 (PET) or Single Photon Emission Computed Tomography (SPECT) activity-based imaging
87 probes could offer a non-invasive tool to early detect and diagnose MMP-related diseases
88 (e.g. colorectal cancer), to elucidate the exact role of specific MMPs in normal and disease
89 states or to understand the mechanism of action of these enzymes. During the last decades
90 several research groups have been developing PET and SPECT probes for MMP-targeted
91 imaging [see 22 for a recent review]. Most of them are however broad spectrum MMP
92 inhibitors and currently there are no successful MMP selective radiotracers available.
93 Consequently, *in vivo* imaging of a particular MMP type activity remains a challenge.

94 Recently, [¹⁸F]BR420 and [¹⁸F]BR351 (Figure 1) have been described to be brain penetrant
95 broad spectrum MMP PET radiotracers with favourable affinities for activated MMP-2 and
96 MMP-9 ([¹⁸F]BR420, IC₅₀ = 7 ± 2 and 23 ± 9 nM; and [¹⁸F]BR351, IC₅₀ = 50 ± 27 and 4 ± 3
97 nM, for MMP-9 and MMP-2, respectively).^{23,24} Both compounds belong to different families
98 of MMP ligands with BR420 being a barbiturate-based MMP inhibitor and BR351, a
99 hydroxamate-based MMP inhibitor. The *in vivo* evaluation of [¹⁸F]BR420 has so far been
100 limited to an *in vivo* biodistribution study up to 2 h p.i. in adult C57/BL6 mice, indicating no
101 tissue specific accumulation of the radiotracer.²³ [¹⁸F]BR351 on the other hand has recently
102 successfully been used to image MMP activity after transient middle cerebral artery occlusion
103 in mice.²⁵ [¹⁸F]BR420 and [¹⁸F]BR351 have not yet been evaluated in an oncology context.
104 Considering the prognostic value of MMP-9 expression in colorectal cancer, the aim of the
105 present study was to evaluate and compare the *in vivo* behaviour of [¹⁸F]BR420 and
106 [¹⁸F]BR351 in a mouse model of human colorectal cancer. The tumour targeting properties
107 were evaluated as well as the *in vivo* stability at several time points post tracer injection. For
108 [¹⁸F]BR420, a novel and improved automated radiosynthesis was developed.

109



111 **Figure 1:** Structures of [¹⁸F]BR420 and [¹⁸F]BR351.

112 2. Experimental

113 2.1. General procedures and materials

114 Unless stated otherwise, all chemical reagents and solvents were obtained from commercial
 115 sources and used without further purification. Characterization of all compounds was
 116 performed by ¹H NMR, ¹³C NMR and mass spectrometry. ¹H NMR and ¹³C NMR spectra
 117 were recorded on a 400 MHz Bruker Advance DRX spectrometer and analysed by use of
 118 MestReNova analytical chemistry software. Chemical shifts are in ppm and coupling
 119 constants are in hertz (Hz). Purities were determined using two different UPLC systems based
 120 either on mass detection or on UV detection: a Waters Acquity UPLC system coupled to a
 121 Waters TUV detector and a Waters TQD ESI mass spectrometer. On both systems, a Waters
 122 Acquity UPLC BEH C18 1.7 μm, 2.1 x 50 mm column was used. Solvent A: water with 0.1 %
 123 formic acid; Solvent B: acetonitrile with 0.1 % formic acid. Method I: 0.7 mL/min, 0.15 min
 124 95 % A, 5% B then in 1.85 min from 95 % A, 5 % B to 10 0% B, 0% A, then 0.25 min, 100
 125 % B, 0 % A, 0.75 min (0.35 mL/min) 95 % A, 5 % B. Method II (purity method): 0.4
 126 mL/min, 0.15 min 95 % A, 5% B then in 4.85 min from 95 % A, 5 % B to 100 % B, 0 % A,
 127 then 0.25 min, 100 % B, 0% A, 0.75 min 95 % A, 5 % B. Where necessary, flash purification
 128 was performed with a Biotage ISOLERA One flash system equipped with an internal variable
 129 dual-wavelength diode array detector (200-400 nm). Biotage® SNAP cartridges were used for
 130 normal phase purification (KP-Sil 10 – 100 g, flow rate: 10 – 100 mL/min). For
 131 radiosynthesis, no carrier-added [¹⁸F] F⁻ was produced by the ¹⁸O(p,n)¹⁸F nuclear reaction in a
 132 Siemens Eclipse HP cyclotron by bombardment of [¹⁸O]H₂O (Rotem Industries, Israel).
 133 Radiosynthesis of [¹⁸F]BR420 and [¹⁸F]BR351 was carried out on an automated synthesis
 134 module (Fluorsynthon I, Comecer Netherlands, The Netherlands) specifically adapted for
 135 these radiosynthesis. Radiochemical yields were calculated from the theoretical initial amount
 136 of [¹⁸F]F⁻ and decay corrected to end of bombardment (EOB). Purification of [¹⁸F]BR420 and

137 [¹⁸F]BR351 following radiosynthesis was performed by reverse phase semi-preparative HPLC
138 using a Knauer HPLC pump and a Smartline UV detector ($\lambda = 254$ nm) in line with a Hi-Rad
139 1000-CD-X CdWO₄ scintillation detector (Scionix, The Netherlands). Radiochemical and
140 chemical purity was determined by analytical reverse phase HPLC using a Shimadzu LC-
141 20AT HPLC pump equipped with a SPD-20A UV/VIS detector (Shimadzu, Japan) in series
142 with a NaI scintillation detector for radiation detection (Raytest, Germany). The recorded data
143 were processed by the GINA-Star 5 software (Raytest, Germany). Radioactivity in samples
144 from animal studies was measured in a Wizard² 2480 automatic gamma counter (Perkin
145 Elmer, Finland).

146 2.2. Chemistry

147 2.2.1. 5-[4-(2-chloroethyl)piperazin-1-yl]-5-(4-phenoxyphenyl)pyrimidine-2,4,6-trione (**1**)

148 *N*-(2-Chloroethyl) piperazine (42%) was prepared as the trifluoroacetic acid salt **3** by the
149 reaction of *N*-Boc piperazine **2** (97%) with bromo-chloroethane. Barbiturate scaffold **4** (67%)
150 was prepared as previously described.²⁶ To a cooled solution of **4** (0.186 g, 0.628 mmol) in
151 DMF (2 mL) at 0 °C, a solution of NBS (0.112 g, 0.628 mmol) in DMF (2 mL) was dropwise
152 added over a period of 15 min. Then, the addition funnel was rinsed with DMF (2 mL) and
153 the rinse was also added to the reaction mixture. After stirring for 20 min, compound **3** (0.165
154 g, 0.628 mmol) and K₂CO₃ (0.174 g, 1.256 mmol) were added and the reaction mixture was
155 stirred at 0 °C for 60 min and then allowed to reach room temperature and stirred for
156 additional 20 h. The reaction mixture was then diluted in EtOAc and an aqueous solution of
157 citric acid (0.628 mmol, 0.1 M) was added. The organic phase was separated and washed with
158 water and brine, dried over Na₂SO₄, filtered and concentrated under reduced pressure. The
159 crude product was purified by manual chromatography (Hexane/EtOAc, 1/2, V/V) to yield
160 compound **1** (0.054 g, 20%). ¹H NMR (400MHz, CDCl₃): δ = 9.18 (bs, 2H), 7.43-7.39 (m,
161 4H), 7.21-7.17 (m, 1H), 7.08-7.02 (m, 4H), 4.25-4.22 (m, 2H), 3.80-3.78 (m, 2H), 3.40-3.34
162 (m, 4H), 2.60-2.56 (m, 4H) ppm. ¹³C NMR (100 MHz, CDCl₃): δ 30.72, 42.94, 64.79, 74.30,
163 78.61, 78.98, 79.26, 118.19, 119.37, 124.19, 128.82, 129.23, 129.56, 130.19, 149.35, 153.55,
164 153.97, 155.70, 157.60, 169.91 ppm. MS (ESI) m/z = 487.2 [M + H + CH₃CN]⁺.

165 2.3. Radiochemistry

166 [¹⁸F]F⁻ was transferred from the cyclotron to the synthesis module and trapped on an activated
167 anion exchange cartridge (QMA Sep-Pak Light, Waters). [¹⁸F]F⁻ was eluted with 1 mL of a

168 solution of Kryptofix 222 (220 mg) and K_2CO_3 (40 mg) in CH_3CN/H_2O (83/17, V/V) and
169 collected in the reaction vial. The solution was evaporated at $130^\circ C$ with a stream of helium
170 (1 bar) and under vacuum for 8 min. To ensure dryness, azeotropic distillation of 1 mL of
171 acetonitrile was performed twice for 6 min at $140^\circ C$ with a stream of helium (1 bar). The
172 reaction was then cooled down to $90^\circ C$ with compressed air and a solution of the precursor **1**
173 (2 mg in 1 mL of DMSO) was added to the reaction vial. The reaction mixture was heated at
174 $120^\circ C$ for 10 min, cooled down to $80^\circ C$ and diluted with 1.9 mL of a solution of 0.05 M
175 NaOAc, pH 5.5 / 96% EtOH (50/50, V/V). This solution was passed through an Alumina N
176 light cartridge (Waters) and injected into the HPLC loop. The crude reaction mixture was
177 purified on a Phenomenex Luna C18, $10\ \mu m$, $10 \times 250\ mm$ column and eluted with a solution
178 of 0.05 M NaOAc, pH 5.5 / 96 % EtOH (50/50, V/V) at 4 mL/min. [^{18}F]BR420 was collected
179 ($R_t = 12$ -13 min), filtered through a $0.22\ \mu m$ sterile filter (PES syringe filter, 25 mm, $0.2\ \mu m$)
180 and diluted with 0.9% sodium chloride solution to reduce the EtOH concentration to $< 10\ %$.
181 Chemical and radiochemical purity of the tracer was measured by analytical HPLC
182 (Phenomenex Luna C18, $5\ \mu m$, $4.6 \times 150\ mm$) eluted with 0.1 % TFA in H_2O / 0.1 % TFA in
183 CH_3CN (55/45, V/V) at a flowrate of 1 mL/min. The specific activity was determined using a
184 UV calibration curve ($\lambda = 272\ nm$).

185 [^{18}F]BR351 was reproduced according to the literature²⁴ with slight modifications. A solution
186 of the precursor **5** (2 mg in 1 mL of CH_3CN) was added to the azeotropically dried [^{18}F]K222F
187 and the reaction mixture was heated at $90^\circ C$ for 20 min, cooled down to $80^\circ C$ and diluted
188 with 1.9 mL of a solution of 0.05 M NaOAc, pH 5.5 / 96 % EtOH (45/55, V/V). This solution
189 was passed through an Alumina N light cartridge (Waters) and injected into the HPLC loop.
190 The crude reaction mixture was purified on a Phenomenex Luna C18, $10\ \mu m$, $10 \times 250\ mm$
191 column and eluted with a solution of 0.05 M NaOAc, pH 5.5 / 96 % EtOH (45/55, V/V) at 3
192 mL/min. [^{18}F]BR351 eluted with a retention time of 10-11 min, was collected, filtered
193 through a $0.22\ \mu m$ sterile filter (PES syringe filter, 25 mm, $0.2\ \mu m$) and diluted with 0.9 %
194 sodium chloride solution to reduce the EtOH concentration to $< 10\ %$. Chemical and
195 radiochemical purity of the tracer was measured by analytical HPLC (Phenomenex Luna C18,
196 $5\ \mu m$, $4.6 \times 150\ mm$) eluted with 0.1 % TFA in H_2O / 0.1 % TFA in CH_3CN (52/48, V/V) at a
197 flowrate of 1 mL/min. The specific activity was determined using a UV calibration curve ($\lambda =$
198 $254\ nm$).

199 2.4. *Cell cultures and animal model*

200 The experimental protocol was approved by the Antwerp University Ethical Committee for
201 Animal Experiments (ECD 2015-13), and all applicable institutional and national guidelines
202 for the care and use of animals were followed. Human colorectal cancer cell line Colo205 was
203 used for induction of xenografts because of its known MMP-9 expression.²⁷ Low-passage
204 Colo205-*luc2* cells (PerkinElmer, Maltham, MA, USA) were cultured in RPMI1640 medium
205 enriched with 10 % FBS, 2 mM L-glutamine, 1 mM sodium pyruvate, and 1 % penicillin-
206 streptomycin (Invitrogen, Merelbeke, Belgium) at 37 °C and 5 % CO₂ in a humidified
207 incubator. For inoculation, cells were harvested by trypsinization with trypsin-EDTA (0.05 %;
208 Invitrogen) and counted with the Muse™ Cell Count and Viability Assay (Merck Millipore,
209 Overijse, Belgium). Colo205 cells were then resuspended in sterile phosphate buffered saline
210 (PBS) at a concentration of 2×10^6 viable cells per 100 μ L for inoculation. Female CD1-/-
211 athymic nude mice aged 6-8 weeks (Charles Rivers, Calco, Italy) were subcutaneously
212 inoculated in both hind legs with 100 μ L of cell suspension. Tumor growth was evaluated
213 three times a week with digital caliper measurements from the moment tumors became
214 palpable. Tumor volume was calculated with the formula $V = 0.5 \times (length \times width^2)$.

215 2.5. *In vivo* μ PET imaging

216 Fully body PET/CT imaging was performed on an Inveon μ PET/CT scanner (Siemens
217 Preclinical Solutions Inc, Knoxville, TN, USA). CD1-/- nude female mice bearing Colo205
218 xenografts were injected intravenously (i.v.) via a catheter in the lateral tail vein with
219 [¹⁸F]BR420 (37.8 MBq, n = 1) or [¹⁸F]BR351 (5.6 ± 3.4 MBq, n = 2) and underwent a 60 min
220 dynamic μ PET scan followed by static scans at 2 h p.i. (20 min) and 4 h p.i. (46 min). For the
221 scan, mice were anesthetized with isoflurane (5% for induction, 2% for maintenance)
222 supplemented with oxygen. PET data was recorded in list-mode format and the 60 min scan
223 was divided in a total of 33 frames: 12 x 10 s, 3 x 20 s, 3 x 30 s, 3 x 60 s, 3 x 150 s and 9 x
224 300 s. The PET images were reconstructed using 2 iterations with 16 subsets of the three-
225 dimensional ordered subset expectation maximization (OSEM) algorithm²⁸ followed by 18
226 maximum a posteriori (MAP) iterations. Normalization, dead time, random, CT-based
227 attenuation and scatter corrections were applied. CT imaging was done using a 220 degrees
228 rotation with 120 rotation steps. Voltage and amperage were set to 80 keV and 500 μ A,
229 respectively.

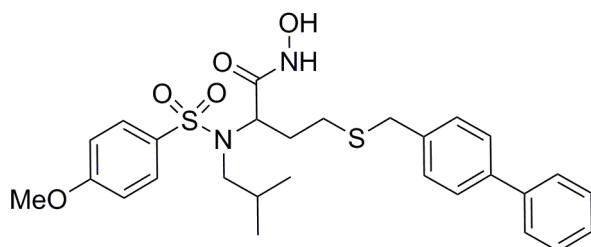
230 Volume-of-interests (VOIs) for the whole tumors, heart (a measure of the blood pool),
231 muscle, liver and kidneys were drawn manually on the co-registered CT images using PMOD

232 v3.3 (PMOD Technologies, Switzerland). Using this VOI the tracer uptake was then obtained
233 and defined as the percent injected dose per cubic centimeter (%ID/cc) = 100 x activity
234 concentration in the VOI (kBq/cc) / the injected dose (kBq).

235 2.6. *Ex vivo biodistribution and blocking study*

236 CD1^{-/-} nude female mice bearing Colo205 xenografts (n = 4 for [¹⁸F]BR420, n = 3 for
237 [¹⁸F]BR351), were i.v. injected with 18.76 ± 1.02 MBq [¹⁸F]BR420 or 5.92 ± 1.23 MBq
238 [¹⁸F]BR351 via the lateral tail vein under isoflurane anesthesia. At 2 h post injection (p.i.),
239 animals were sacrificed by cervical dislocation to perform *ex vivo* biodistribution. Blood was
240 collected via cardiac puncture and thereafter tumors and main organs were rapidly removed,
241 rinsed in PBS, blotted dry and measured. The uptake of radioactivity in blood and organs was
242 expressed as percentage of the injected dose per gram of tissue plus or minus the standard
243 deviation (%ID/g ± SD).

244 A blocking study was performed for [¹⁸F]BR420 (n = 4), using a different and more potent
245 MMP-9 ligand (IC₅₀ = 0.2 nM for MMP-9; 20 nM for MMP-3; 30 nM for MMP-2) (Figure
246 2).²⁹ The blocking agent was injected 30 min before the radiotracer at a dose of 1 mg/kg. Two
247 hours p.i. (6.66 ± 1.68 MBq), the animals were sacrificed. Blood, tumors and main organs
248 were collected, weighed and counted as described above.



249

250 **Figure 2:** Structure of the MMP-9 blocking agent.

251 2.7. *Plasma metabolite analysis*

252 Plasma radiometabolite analysis was performed at 2 h p.i. for [¹⁸F]BR420 (n = 4, 5.72 ± 0.24
253 MBq) and at 5 min, 15 min, 30 min and 2 h p.i. for [¹⁸F]BR351 (n = 3 per time point, 14.41 ±
254 5.72 MBq). At the indicated time points, mice were sacrificed and blood (500-800 µL,
255 withdrawn by cardiac puncture) was centrifuged at 4°C for 7 min at 4000 rpm. The plasma
256 was removed (200-300 µL) and the same amount of ice-cold CH₃CN was added followed by
257 addition of 10 µL of a solution of the cold standard (BR420 or BR351, 1 mg/mL). The sample

258 was counted in the automatic gamma-counter and vortexed for 30 s. Following centrifugation
259 for 4 min at 4000 rpm, the supernatant was separated from the pellet. Subsequently, both
260 fractions were counted in the gamma-counter to calculate the extraction efficiency (%
261 recovery of radioactivity in CH₃CN). Hundred μL of the supernatant was analyzed by reverse
262 phase HPLC using a Phenomex Luna (C18, 5 μm, 4.6 mm x 150 mm) column eluted with 0.1
263 %TFA in H₂O/0.1 % TFA in CH₃CN (55/45, V/V for [¹⁸F]BR420; 52/48, V/V for
264 [¹⁸F]BR351) at a flow rate of 1 mL/min. The HPLC column was coupled to a Phenomenex
265 guard column. Fractions were automatically collected every 30 s and measured with the
266 gamma-counter. A validation study for metabolite analysis was also performed to exclude
267 degradation of the radiotracer during work-up. For this, an aliquot of the radiotracer was
268 added to blood *in vitro* and the samples were processed as described for the metabolite
269 analysis and analyzed by HPLC.

270 2.8. *Ex vivo autoradiography, immunohistochemistry and in situ zymography*

271 Immediately after gamma counting, the tumors were snap-frozen in cooled isopentane (-35°C)
272 and sectioned. Serial cryosections were collected in triplicate for *ex vivo* autoradiography (20
273 μm), immunohistochemistry (20 μm) and *in situ* zymography (10 μm).

274 For *ex vivo* autoradiography, 20 μm fresh-frozen sections were exposed overnight to high-
275 sensitivity phosphor imaging plates and subsequently scanned using the Fujifilm image reader
276 FLA-7000.

277 Immunohistochemical staining of MMP-9 and MMP-2 was performed on 20 μm fresh-frozen
278 sections using respectively a rabbit polyclonal anti-MMP-9 antibody (ab38898, Abcam, UK)
279 and a rabbit polyclonal anti-MMP-2 antibody (ab37150, Abcam, UK). Tumor sections were
280 fixed using 4% paraformaldehyde and washed with PBS. Non-specific binding was blocked
281 using 3% hydrogen peroxide and 3% Normal Goat Serum (Jackson ImmunoResearch, UK).
282 3% Bovine Serum Albumin (Sigma-Aldrich, Belgium) was included in the blocking step for
283 immunohistochemical staining of MMP-2. Sections were incubated overnight with the
284 primary antibody, diluted 1:1000 (anti-MMP-9) or 1:500 (anti-MMP-2) in antibody diluent
285 containing 0.1% Bovine Serum Albumin, 0.2% Triton X-100 (Sigma-Aldrich, Belgium) and
286 2% Normal Goat Serum. The following morning, sections were washed and incubated for 1 h
287 with horse radish peroxidase-conjugated secondary antibody (goat anti-rabbit; 1:500; Jackson
288 ImmunoResearch, UK). Finally, sections were exposed for 10 min to the colorimetric
289 substrate 3,3'-diaminobenzidine (Dako, Denmark). The tumor sections were counterstained

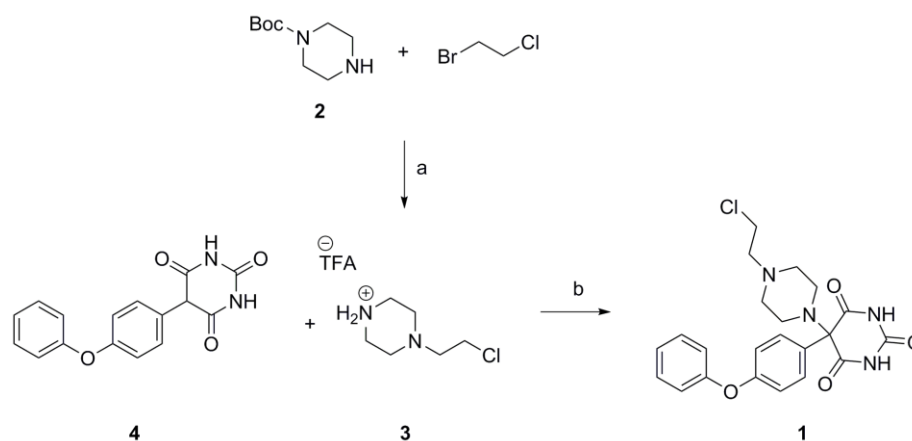
290 with cresyl violet, dehydrated and coverslipped. Images were obtained using an Olympus
291 CX31 light microscope (Olympus Corporation, Japan) equipped with an AxioCam Erc 5s
292 camera (Zeiss, Germany). ZEN 2012 software (Zeiss, Germany) was used for image
293 acquisition.

294 *In situ* zymography was performed to assess gelatinase activity (MMP-9 and MMP-2) in the
295 same tumor tissue. 10 μ m fresh-frozen sections were pre-incubated in water at 37°C for 100
296 min and subsequently covered with a fluorogenic substrate DQ gelatin (DQ gelation from pig
297 skin, fluorescein conjugate, Life Technologies/Molecular Probes, USA), which was diluted
298 1:100 in the buffer supplied by the manufacturer, at 37°C for 45 min. After washing, sections
299 were mounted using VECTASHIELD mounting medium with DAPI (Vector Laboratories,
300 USA) and coverslipped. To examine the specificity of the reaction, 10 mM 1,10-phenantroline
301 (Life Technologies/Molecular Probes, USA), a chelator and general MMP inhibitor, was
302 added to the pre-incubation and reaction steps in sections adjacent to those used for the
303 normal *in situ* zymography. Images were acquired at room temperature using an Olympus
304 BX51 fluorescence microscope equipped with PlanC-N 4x/0.10 and UplanFL-N 20x/0.5
305 objective lenses and an Olympus DP71 digital camera. Olympus cellSens Dimension software
306 was used for image acquisition and processing.

307 **3. Results and discussion**

308 *3.1. Chemistry*

309 Cold standard BR420 was synthesized in a moderate yield (38%) following the published
310 methodology.²³ Since the two-step radiosynthesis of [¹⁸F]BR420 according to the reported
311 method²³ failed in our hands, alternative one-step radiolabeling procedures using different
312 precursors were explored. First the synthesis of a tosylate derivative was evaluated. The
313 synthesis of the labelling precursor however failed most likely because tosylation/mesylation
314 of the primary alcohol results in a highly unstable aziridinium salt which undergoes a ring-
315 opening reaction to yield the starting alcohol.³⁰ We therefore decided to prepare chloro-
316 derivative **1** as alternative precursor for the one-step radiosynthesis of [¹⁸F]BR420 following
317 the synthetic pathway described in Scheme 1.

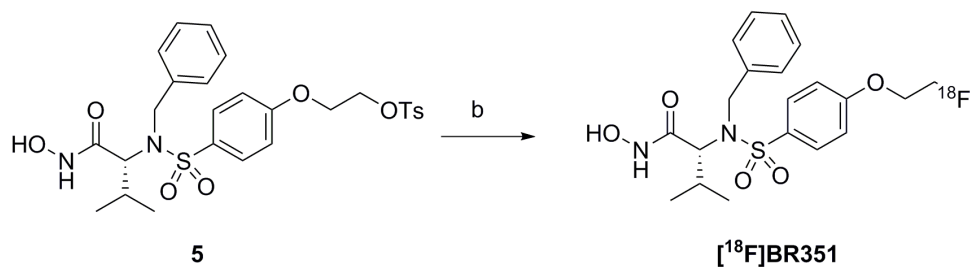
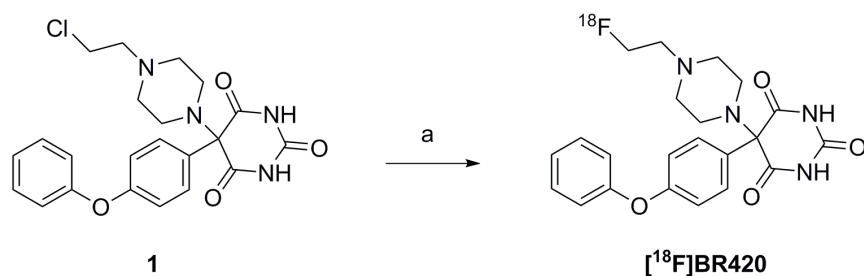


318
 319 **Scheme 1:** Synthesis of precursor **1**. Reagents and conditions: (a) i) Cs₂CO₃, DMF, rt, 3d; ii)
 320 TFA, DCM, 0°C-rt; (b) NBS, K₂CO₃, DMF, 5°C-rt.

321 Cold standard BR351 and the corresponding precursor **5** were reproduced as previously
 322 described in the literature²⁴ in moderate yields of 38% and 54%, respectively.

323 3.2. Radiochemistry

324 While evaluating the two-steps radiosynthesis of [¹⁸F]BR420 described in literature²³ radio-
 325 HPLC analysis of the second step (reaction of the 1-[¹⁸F]fluoro-2-tosyloxyethane with the
 326 piperazine-containing barbiturate scaffold) at different time points indicated formation of
 327 several byproducts while [¹⁸F]BR420 could not be obtained. By implementing a one-step
 328 approach using direct displacement of the chloro derivative **1** by [¹⁸F]fluoride (Scheme 2),
 329 [¹⁸F]BR420 could be successfully obtained in a radiochemical yield of 16.22 ± 3.12% (n = 10,
 330 decay-corrected to EOB). By using a biocompatible mobile phase for HPLC purification of
 331 the reaction mixture a simple dilution and sterile filtration step could be used to obtain an
 332 injection-ready solution of [¹⁸F]BR420, thereby reducing the total synthesis to 60 min (EOB),
 333 including formulation. Chemical and radiochemical purity were > 98% and the determined
 334 specific activity was 65.07 ± 27.63 GBq/μmol (EOS, n = 10).



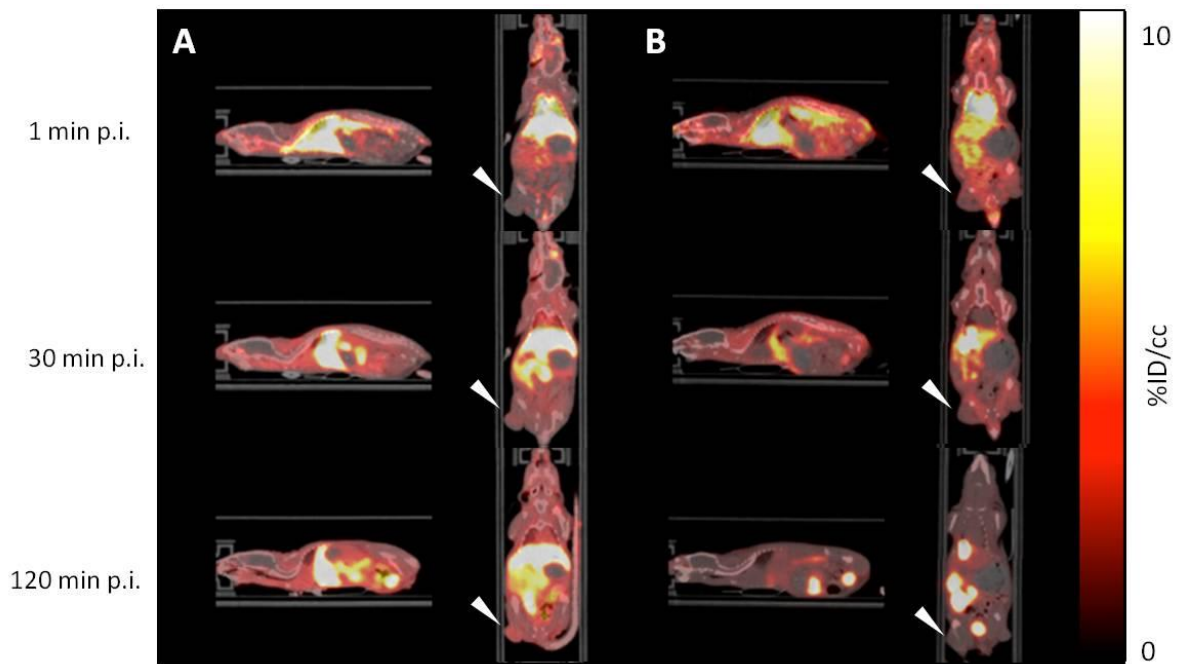
335

336 **Scheme 2:** Fully automated synthesis of [¹⁸F]BR420 and [¹⁸F]BR351. Reagents and
 337 conditions: (a) [¹⁸F]Fluoride, K₂CO₃, Kryptofix-2.2.2, DMSO, 120°C, 10 min; (b)
 338 [¹⁸F]Fluoride, K₂CO₃, Kryptofix-2.2.2, CH₃CN, 90°C, 20 min.

339 Radiosynthesis of [¹⁸F]BR351 was performed as previously reported²⁴ by reaction of tosylate
 340 precursor **5** dissolved in CH₃CN with dried [¹⁸F]F⁻ for 20 min at 90°C (Scheme 2). Again, a
 341 biocompatible mobile phase was used for the purification, omitting the need for an extra Sep-
 342 Pak purification step. Purified [¹⁸F]BR351 could be obtained in a decay corrected
 343 radiochemical yield of 22.42 ± 12.79% (n = 5), in a total synthesis time of 70 min (EOB),
 344 including formulation, and with a radiochemical purity > 98%. The determined specific
 345 activity was 172.0 ± 153.10 GBq/μmol (EOS, n = 5).

346 3.3. Exploratory *in vivo* μPET imaging study

347 An *ex vivo* biodistribution study at different time points up to 60 min post injection of
 348 [¹⁸F]BR351 as well as a μPET imaging study up to 2 h post injection of [¹⁸F]BR420 in normal
 349 C57/BL6 mice have previously been published.^{23,24} These studies indicated low uptake for
 350 both tracers in heart, brain, lung and muscle with clearance of radioactivity out of excretory
 351 organs such as liver and kidneys with time after injection. Therefore in the current study, only
 352 a limited number of animals was evaluated by μPET imaging to enable the selection of a time
 353 point for a more elaborate *ex vivo* evaluation of tumor uptake and tracer stability.

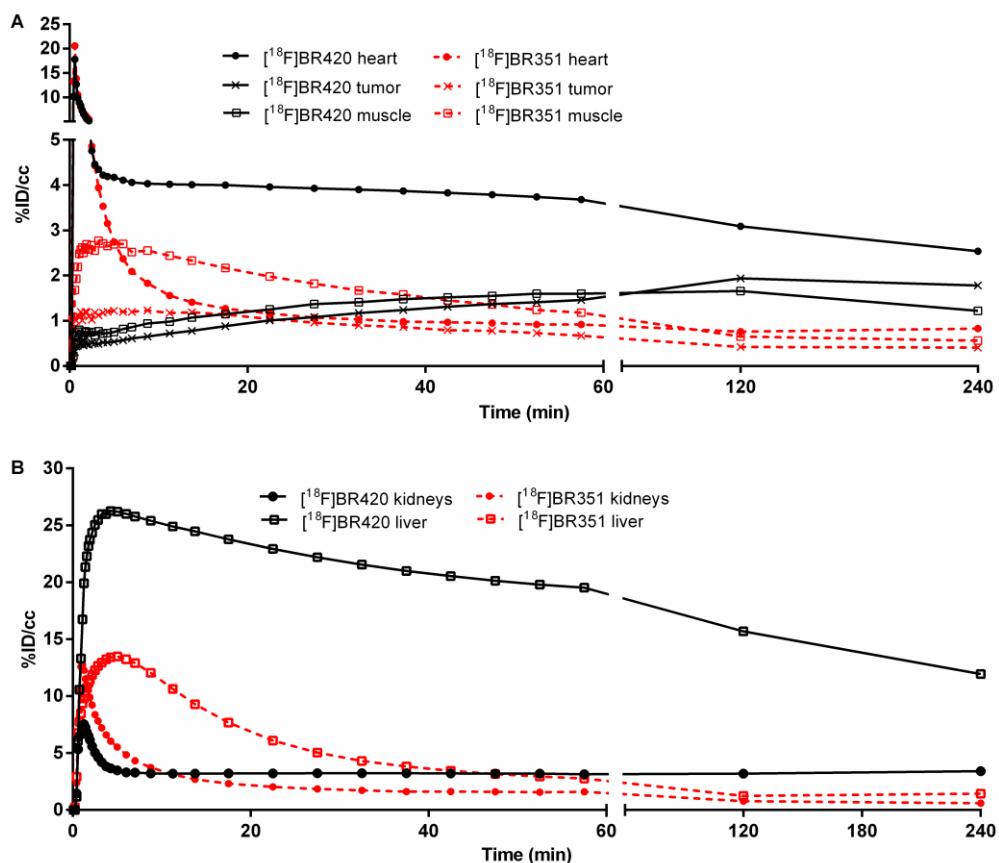


354

355 **Figure 3:** Representative μ PET/CT images of CD1^{-/-} athymic nude mice intravenously
 356 injected with 38 MBq [¹⁸F]BR420 (n = 1) (A) or 6 MBq [¹⁸F]BR351 (n = 2) (B). PET images
 357 are presented in sagittal and coronal orientation at 1 min, 30 min and 2h post tracer injection.
 358 Tumors are pointed with arrow heads.

359 Representative μ PET/CT images are presented in Figure 3. For [¹⁸F]BR420 tumor uptake
 360 increased from 0.45 %ID/cc at 1 min p.i. to a maximum value of 1.94 %ID/cc at 2 h post
 361 tracer injection with little decrease in uptake up to 4h post injection (1.78 %ID/cc) (Figure 4).

362



363

364 **Figure 4:** Time-Activity curve (%ID/cc) for heart, tumor and muscle (A) and kidneys and
 365 liver (B) of CD1^{-/-} athymic nude mice injected with $[^{18}\text{F}]\text{BR420}$ (n = 1) or $[^{18}\text{F}]\text{BR351}$ (n =
 366 2).

367 For $[^{18}\text{F}]\text{BR351}$, an initial higher tumor uptake of 1.11 %ID/cc was detected at 1 min p.i.
 368 which increased to a maximum uptake of 1.23 %ID/cc at 9 min p.i.. Tumor uptake then
 369 decreased to 0.42 %ID/cc at 2 h p.i. and remained stable up to 4 h p.i. (0.41 %ID/cc). In
 370 contrast to $[^{18}\text{F}]\text{BR420}$ for which tumor uptake exceeded uptake in the muscle at 2h p.i. (1.66
 371 %ID/cc in the muscle) and 4h p.i. (1.22 %ID/cc in the muscle), tumor uptake of $[^{18}\text{F}]\text{BR351}$
 372 did not exceed uptake in the muscle at any of the investigated time points. $[^{18}\text{F}]\text{BR420}$
 373 demonstrated a slow blood clearance with an initial peak uptake of 17.78 %ID/cc in the heart
 374 decreasing to 5.53 %ID/cc at 2 min p.i., 3.90 %ID/cc at 30 min p.i. and 3.09% ID/cc at 2h p.i..
 375 For $[^{18}\text{F}]\text{BR351}$ an initial higher peak uptake of 20.56 %ID/cc was detected in the heart
 376 followed by a faster wash-out compared to $[^{18}\text{F}]\text{BR420}$ (5.93 %ID/cc at 2 min p.i., 1.03
 377 %ID/cc at 30 min p.i. and 0.76 %ID/cc at 2 h p.i.). For $[^{18}\text{F}]\text{BR420}$ highest uptake could be
 378 detected in the liver (26.27 %ID/cc at 4 min p.i. and 15.69 %ID/cc at 2 h p.i.) indicating
 379 predominant hepatobiliary clearance of the tracer. For $[^{18}\text{F}]\text{BR351}$ lower (13.24 %ID/cc at 4

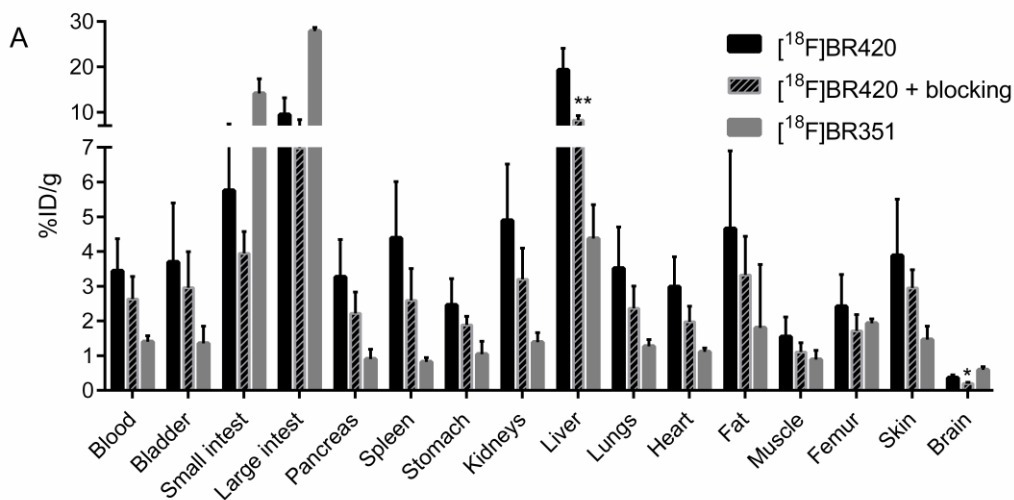
380 min p.i. and 1.25 %ID/cc at 2 h p.i.) but also predominant hepatobiliary clearance could be
381 detected. In the previously reported μ PET study of [^{18}F]BR420 in C57/BL6 mice an initial
382 high liver uptake was demonstrated but in contrast to our study, the liver uptake decreased
383 with at 2 h p.i. uptake mainly being visible in intestines and bladder.²³ The slower clearance
384 from the liver seen in our study might be related to a mouse strain difference. For [^{18}F]BR351
385 an *ex vivo* biodistribution study in C57/BL6 mice indicated predominant hepatobiliary
386 clearance at 60 min post tracer injection²⁴ which is comparable to the excretion profile
387 witnessed in our study.

388 3.4. *Ex vivo* evaluation of tumor uptake

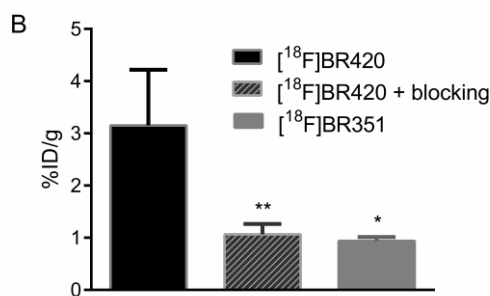
389 For a more elaborate comparison of tumor uptake and stability of [^{18}F]BR420 and [^{18}F]BR351
390 the 2 h p.i. time point was selected as the exploratory μ PET imaging study indicated clearance
391 of radioactivity from non-target organs at 2 h p.i. while tumor uptake stabilized. The 2 h p.i.
392 time point was also the time point demonstrating the highest tumor uptake which was attained
393 for [^{18}F]BR420. Distribution of ^{18}F radioactivity in various organs at 2 h p.i. following iv
394 administration of [^{18}F]BR420 (with and without blocking) and [^{18}F]BR351 is presented in
395 Figure 5. As was also visible in the μ PET imaging, [^{18}F]BR420 displays a slower blood
396 clearance compared to [^{18}F]BR351 with 3.44 ± 0.93 %ID/g remaining in the blood at 2 h p.i.
397 for [^{18}F]BR420 versus 1.40 ± 0.17 %ID/g for [^{18}F]BR351. For [^{18}F]BR420 the biodistribution
398 study showed a large accumulation of the tracer in the liver (19.33 ± 4.76 %ID/g) and large
399 intestines (9.49 ± 3.70 %ID/g), while for [^{18}F]BR351 the highest uptake could be detected in
400 large and small intestines (27.90 ± 0.79 and 14.14 ± 3.22 %ID/g, respectively) (Figure 5A).
401 Tumor uptake was significantly higher for [^{18}F]BR420 (3.15 ± 0.03 %ID/g versus $0.94 \pm$
402 0.18 %ID/g for [^{18}F]BR351, $p < 0.05$, Figure 5B). The slow blood clearance of [^{18}F]BR420
403 resulted in low a tumor-to-blood (T/B) ratio of 0.92 and a tumor-to-muscle (T/M) ratio of
404 2.03. T/B and T/M ratios for [^{18}F]BR351 were 0.67 and 1.06, respectively.

405 As the best tumor accumulation was obtained for [^{18}F]BR420, a blocking study was
406 performed to evaluate MMP-9 selectivity of the tumor signal. Pre-treatment of the animals
407 with a more potent MMP-9 inhibitor resulted in a significant decrease in [^{18}F]BR420 uptake
408 in the tumor ($p < 0.01$) (Figure 5B). Administration of the blocking agent also influenced the
409 tracer uptake in all other organs with a significant reduction of tracer accumulation observed
410 for liver ($p < 0.01$) and brain ($p < 0.05$). This might be related to constitutive physiological

411 expression of MMPs in normal tissue, reflecting the broad spectrum of both [¹⁸F]BR420 and
 412 our blocking agent.



413



414

415 **Figure 5:** *Ex vivo* biodistribution (%ID/g ± SD) in selected organs (A) and tumors (B) at 2 h
 416 p.i. of [¹⁸F]BR420 (n = 4 for non blocked and blocked) or [¹⁸F]BR351 (n = 3). Statistical
 417 analysis was performed by unpaired two-tailed t-test, * p < 0.05, ** p < 0.01, significantly
 418 different from non-blocked.

419 3.5. Plasma metabolite analysis

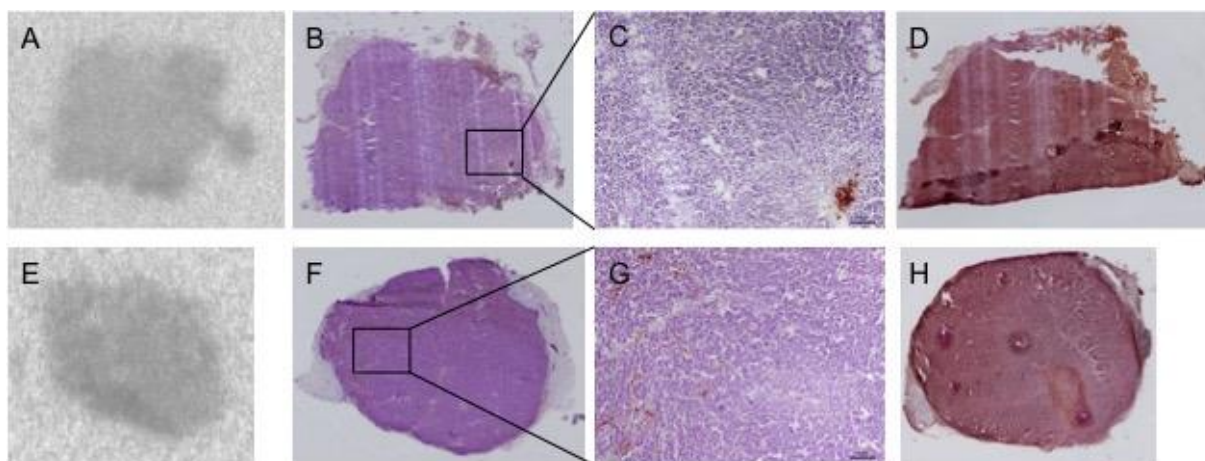
420 A possible explanation for the higher tumor uptake of [¹⁸F]BR420 compared to [¹⁸F]BR351
 421 could be its lower binding affinity for MMP-9 (IC₅₀ = 50 ± 27 nM versus 7 ± 2 nM for
 422 [¹⁸F]BR420), the faster blood clearance of [¹⁸F]BR351, or a lower stability compared to
 423 [¹⁸F]BR420 resulting in a reduced tumor accumulation. A plasma metabolite study was
 424 therefore performed to analyse the *in vivo* stability of both tracers. The metabolite validation
 425 assay demonstrated high extraction yields (93.06 ± 0.69% for [¹⁸F]BR420 and 94.75 ± 1.48%
 426 for [¹⁸F]BR351) indicating limited or reversible binding to plasma proteins. No degradation of
 427 the radiotracers was observed during work-up.

428 The radio-HPLC metabolite analysis for [¹⁸F]BR420 revealed high stability of the radiotracer
429 in plasma at 2 h p.i following iv injection, where the concentration of unmetabolized
430 [¹⁸F]BR420 ($t_R = 8.5$ min) represented $86.18 \pm 3.12\%$ of the total radioactivity. Three minor
431 radiometabolite peaks could be detected eluting with retention times of 2 min (M1, $7.02 \pm$
432 2.76%), 4 min (M2, $1.96 \pm 0.32\%$) and 10 min (M3, $5.60 \pm 0.68\%$), respectively. Extraction
433 yield for plasma remained high ($91.32 \pm 1.10\%$).

434 For [¹⁸F]BR351 on the other hand, the radio-HPLC metabolite analysis of plasma indicated
435 only $6.95 \pm 0.95\%$ of intact tracer remaining at 2 h p.i. Additional time points were therefore
436 analyzed indicating a fast metabolism with almost 50% of the tracer being metabolized as
437 early as 5 min p.i. (Table 1). At 15 min p.i. the concentration of unmetabolized [¹⁸F]BR351
438 ($t_R = 7$ min) represented only $20.28 \pm 5.41\%$ of the total radioactivity. Two polar
439 radiometabolites were detected in the plasma, eluting at 2 min (M1) and 3.5 min (M2). The
440 presence of metabolite M1 increased with time p.i. and it became the main radiometabolite
441 peak at 2 h p.i. ($80.45 \pm 3.24\%$). M1 was identified as 2-[¹⁸F]fluoroethanol, a known brain
442 penetrant metabolite, by injection of a solution of 2-fluoroethanol under the same HPLC
443 conditions. Extraction yields for plasma remained relatively constant and high ($85.50 \pm$
444 5.27%) at all investigated time points. A plasma metabolite study by Wagner et al. reported
445 86% of intact [¹⁸F]BR351 remaining at 2.5 min p.i. and 37% at 20 min p.i. with formation of
446 two polar metabolites.²⁴ The much lower plasma stability observed in our study might be
447 mouse strain related or might be attributed to different HPLC conditions used for the analysis.
448 Wagner et al did not identify the major metabolite that was formed, but assumed phase-I
449 metabolism and thus *O*-dealkylation of the parent compound, resulting in 2-[¹⁸F]fluoroethanol
450 to be the mechanism of metabolite generation. This was confirmed in the current study by co-
451 elution with 2-fluoroethanol.

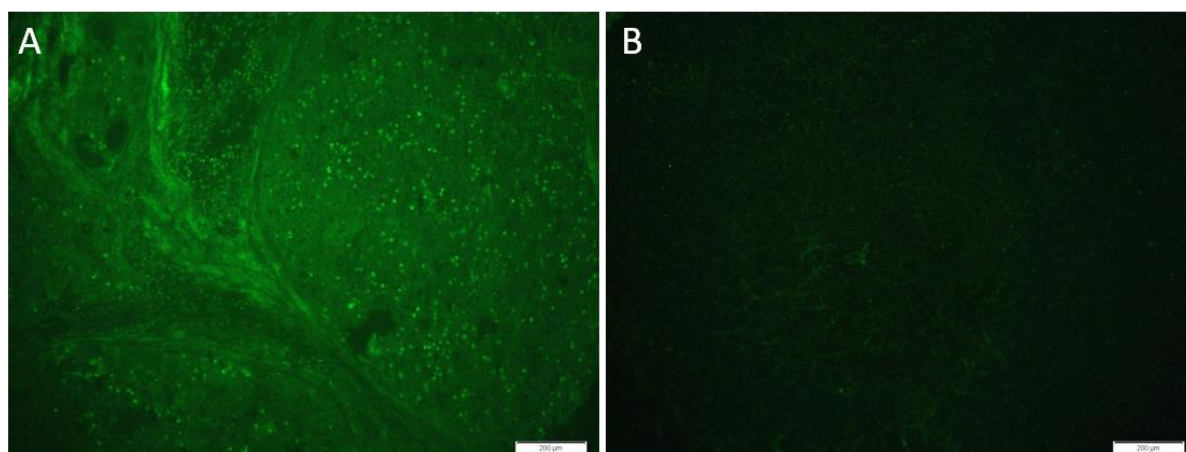
452 3.6. *Ex vivo autoradiography, immunohistochemistry and in situ zymography*

453 As both [¹⁸F]BR351 and [¹⁸F]BR420 are broad spectrum MMP-inhibitors, yet with favourable
454 affinities for activated MMP-2 and MMP-9, the presence of MMP-9 and MMP-2 in the tumor
455 tissue was assessed by immunohistochemistry. MMP-9 was sparsely present in the stroma of
456 the tumor (Figure 6B-C and F-G). MMP-2 immunostaining on the other hand demonstrated a
457 higher expression and homogeneous distribution of MMP-2 throughout the tumor tissue
458 (Figure 6D and H).



459
 460 **Figure 6:** *Ex vivo* autoradiography and immunohistochemical staining of MMP-9 and MMP-
 461 2 in the tumor tissue. A-E: Representative *ex vivo* autoradiographs of respectively [¹⁸F]BR420
 462 (A) and [¹⁸F]BR351 (E) uptake in Colo205 tumor tissue at 2 h p.i.. *Ex vivo* autoradiography
 463 reveals a homogeneous distribution of both radiotracers in the tumors. B-C-F-G: MMP-9
 464 immunostaining reveals sparse expression of MMP-9 in the stroma of the tumor. **B-F: 4x**
 465 **magnification; C-G: 10x magnification, scale bar = 10μm.** D-H: MMP-2 immunostaining
 466 reveals a high and homogeneous expression of MMP-2 throughout the tumor.

467 *In situ* zymography revealed gelatinolytic activity in the tumor tissue (Figure 7A).
 468 Gelatinolytic activity could be blocked by adding 1,10-phenanthroline, a zinc chelator (Figure
 469 7B).



470
 471 **Figure 7:** Gelatinolytic activity in Colo205 tumor tissue. Fluorescence micrographs of *in situ*
 472 zymography with DQ gelatin as fluorogenic substrate (green) in the absence (A) and presence
 473 (B) of 10 mM 1,10-phenanthroline, a general MMP inhibitor. Scale bar = 200 μm.

474 *Ex vivo* autoradiography of tumor slices revealed a homogeneous distribution of both
475 radiotracers in tumor tissue (Figure 6A and E). Although in the blocking study a significant
476 reduction in [¹⁸F]BR420 tumor uptake could be obtained by pre-treatment with a more potent
477 MMP-9 inhibitor, indicating possible selective binding of [¹⁸F]BR420 to MMP-9, the
478 discrepancy between radioactivity distribution of [¹⁸F]BR420 in the autoradiography analysis
479 and the distribution of MMP-9 in the IHC analysis does not support selective binding of the
480 tracer to MMP-9. As the tracer distribution in the tumor is more correlated with MMP-2 IHC
481 and since the blocking agent also has a relative affinity for MMP-2 (IC₅₀ = 30 nM versus 24
482 nM for [¹⁸F]BR420), the reduction in [¹⁸F]BR420 uptake in the tumor might also be related to
483 MMP-2 binding. However, the homogeneous distribution might as well just reflect a broad
484 spectrum binding profile.

485 **4. Conclusion**

486 MMP-9 plays an important role in cancer migration, invasion and metastasis. The availability
487 of a MMP-9 selective radiotracer could aid in drug development, diagnosis and staging of
488 tumors with known MMP-9 expression, including colorectal cancer. Here we present the first
489 evaluation of [¹⁸F]BR420 and [¹⁸F]BR351 as potential MMP-9 PET radiotracers in a
490 colorectal cancer model expressing MMP-9. Preparation of [¹⁸F]BR420 was improved using a
491 novel, faster and fully automated strategy. [¹⁸F]BR351 was quickly metabolized and displayed
492 only low tumor uptake. These unpromising results make [¹⁸F]BR351 not suited for MMP
493 imaging in mouse models of cancer. [¹⁸F]BR420 showed a significantly higher tumor uptake
494 compared to [¹⁸F]BR351 and was found to be stable in plasma up to 2 h p.i. Nevertheless, due
495 to a low T/B ratio and discrepancy of tracer distribution in the tumor with MMP-9
496 immunostaining [¹⁸F]BR420 will not be useful for selective *in vivo* imaging of MMP-9
497 imaging in colorectal cancer.

498 **Acknowledgments**

499 The authors are thankful to Caroline Berghmans and Philippe Joye for technical support. This
500 work has been funded by the ERA-NET NEURON and the University of Antwerp with a
501 BOF research grant (KP 2014 Vazquez N) and Stephan Missault's PhD fellowship of the
502 Research Foundation Flanders (FWO 11K3714N).

503 **References**

504 [1] Birkedal-Hanse, H.; Moore, W. G. I.; Bodden, M. K.; Windsor, L. J.; Birkedal-Hansen, B.;
505 DeCarlo, A.; Engler, J. A. Matrix metalloproteinases: a review. *Crit Rev Oral Biol Med* 1993;
506 4:197-250.

507 [2] Yong, V. W.; Power, C.; Forsyth, P.; Edwards, D. R. Metalloproteinases in biology and
508 pathology of the nervous system. *Nat Rev Neurosci* 2001; 7:502-511.

509 [3] Stamenkovic, I. Matrix metalloproteinases in tumor invasion and metastasis. *Semin*
510 *Cancer Biol* 2000; 10:415-433.

511 [4] Manello, F.; Tonti, G.; Papa, S. Matrix metalloproteinase inhibitors as anticancer
512 therapeutics. *Curr Cancer Drug Targets* 2005; 4:285-298.

513 [5] Curran, S.; Murray, G. I. Matrix metalloproteinases: molecular aspects of their roles in
514 tumor invasion and metastasis. *Eur J Cancer* 2000; 36:1621-1630.

515 [6] Mobasher, A. Osteoarthritis year 2012 in review: biomarkers. *Osteoarthr Cartilage* 2012;
516 20:1451-1464.

517 [7] Folgueras, A. R.; Pendas, A. M.; Sanchez, L. M.; Lopez-Otin, C. Matrix
518 metalloproteinases in cancer: from new functions to improved inhibition strategies. *Int J Dev*
519 *Biol* 2004; 48:411-424.

520 [8] Vihinen, P.; Ala-aho, R.; Kahari, V. M. Matrix metalloproteinases as therapeutic targets in
521 cancer. *Curr Cancer Drug Tar* 2005; 5:203-220.

522 [9] Tziakas, D. N.; Chalikias, G. K.; Stakos, D.; Chatzikyriakou, S. V.; Papazoglou, D.;
523 Mitrousi, K.; Lantzouraki, A.; Thomaidi, A.; Boudoulas, H.; Konstantinides, S. Independent
524 and additive prognostic ability of serum carboxy-terminal telopeptide of collagen type-I in
525 heart failure patients: a multi-marker approach with high-negative predictive value to rule out
526 long-term adverse events. *Eur J Prev Card* 2012; 19:62-71.

527 [10] Mc Cawley, L. J.; Matrisian, L. . Matrix metalloproteinases: multifunctional contributors
528 to tumor progression. *Mol Med Today* 2000; 4:149-156.

529 [11] Yoshizaki, T.; Sato, H.; Furukawa, M. Recent advances in the regulation of matrix
530 metalloproteinase 2 activation: from basic research to clinical application. *Oncol Rep* 2002;
531 9:607-611.

532 [12] Klein, G.; Vellenga, E.; Fraaije, M. W.; Kamps, W. A.; de Bont, E. S. The possible role
533 of matrix metalloproteinase MMP-2 and MMP-9 in cancer, e.g. acute leukemia. *Crit Rev*
534 *Oncol Hematol* 2004; 2:87-100.

535 [13] Konstantinopoulos, P. A.; Karamouzis, M. V.; Papatsoris, A. G.; Papavassiliou, A. G.
536 Matrix metalloproteinase inhibitors as anticancer agents. *Int J Biochem Cell Biol* 2008;
537 40:1156-1168.

538 [14] Leeman, M. F.; Curran, S.; Murray, G. I. New insights into the roles of matrix
539 metalloproteinases in colorectal cancer development and progression. *J Pathol* 2003; 4:528-
540 534.

541 [15] Gonzalez-Pons, M.; Cruz-Correa, M. Colorectal cancer biomarkers: where are we now?
542 *Biomed Res Int* 2015; 1-14.

543 [16] Siegel, R.; DeSantis, C.; Jemal, A. Colorectal cancer statistics, 2014. *CA Cancer J Clin*
544 2014; 64:104-117.

545 [17] Zucker, S.; Vacirca, J. Role of matrix metalloproteinases (MMPs) in colorectal cancer.
546 *Cancer Metastasis Rev* 2004; 23:101-117.

547 [18] Matter, H.; Schudok, M. Recent advances in the design of matrix metalloproteinase
548 inhibitors. *Curr Opin Drug Discov Devel* 2004; 7:513-535.

549 [19] Cuniasse, P.; Devel, L.; Makaritis, A.; Beau, F.; Georgiadis, D.; Matziari, M.; Yiotakis,
550 A.; Dive, V. Future challenges facing the development of specific active-site-directed
551 synthetic inhibitors of MMPs. *Biochimie* 2005; 87:393-402.

552 [20] Schwegmann, K.; Bettenworth, D.; Hermann, S.; Faust, A.; Poremba, C.; Foell, D.;
553 Schäfers, M.; Domagk, D.; Lenz, P. Detection of early murine colorectal cancer by MMP-2/-
554 9-guided fluorescence endoscopy. *Inflamm Bowel Dis* 2016; 22:82-91.

555 [21] Bettenworth, D.; Mücke, M. M.; Schwegmann, K.; Faust, A.; Poremba, C.; Schäfers, M.;
556 Domagk, D.; Lenz, P. Endoscopy-guided orthotopic implantation of colorectal cancer cells
557 results in metastatic colorectal cancer in mice. *Clin Exp Metastasis* 2016; 33:551-562.

558 [22] Matusiak, N.; van Waarde, A.; Bischoff, R.; Oltenfreiter, R.; van de Wiele, C.; Dierckx,
559 R. A. J. O.; Elsinga, P. H. Probes for non-invasive matrix metalloproteinases-targeted imaging
560 with PET and SPECT. *Curr Pharm Des* 2013; 19:4647-4672.

561 [23] Breyholz, H. J.; Wagner, S.; Faust, A.; Rieman, B.; Höltke, C.; Hermann, S.; Schober,
562 O.; Schäfers, M.; Kopka, K. Radiofluorinated pyrimidine-2,4,6-triones as molecular probes
563 for noninvasive MMP-targeted imaging. *Chem Med Chem* 2010; 5:777-789.

564 [24] Wagner, S.; Breyholz, H. J.; Law, M. P.; Faust, A.; Höltke, C.; Schröer, S.; Haufe, G.;
565 Levkau, B.; Schober, O.; Schäfers, M.; Kopka, K. Novel fluorinated derivatives of the broad-
566 spectrum MMP inhibitors N-hydroxy-2(R)-[[[4-methoxyphenyl)sulfonyl](benzyl)- and (3-
567 picolyl)-amino]-3-methyl-butanamide as potential tools for the molecular imaging of
568 activated MMPs with PET. *J Med Chem* 2007; 50:5752-5764.

569 [25] Zinnhardt, B.; Viel, T.; Wachsmuth, L.; Vrachimis, A.; Wagner, S.; Breyholz, H. J.;
570 Faust, A.; Hermann, S.; Kopka, K.; Faber, C.; Dolle, F.; Pappata, S.; Plana, A. M.; Tavitian,
571 B.; Schäfers, M.; Sorokin, L. M.; Kuhlmann, M. T.; Jacobs, A. H. Multimodal imaging

572 reveals temporal and spatial microglia and matrix metalloproteinase activity after
573 experimental stroke. *J Cereb Blood Flow Metab* 2015; 35:1711-1721.

574 [26] Hutchings, S.; Liu, W.; Radinov, R. Palladium-catalyzed arylation of diisopropyl
575 malonate applied to the efficient synthesis of the selective MMP inhibitor 5-(4-
576 phenoxyphenyl)-5-[4-(2-pyrimidinyl)-1-piperazinyl]barbituric acid. *Heterocycles* 2006; 67:
577 763-768.

578 [27] Liang, W.; Kujawaski, M.; Wu, J.; Lu, J.; Hermann, A.; Loera, S.; Yen, Y.; Lee, F.; Yu,
579 H.; Wen, W.; Jove, R. Antitumor activity of targeting Src kinases in endothelial and myeloid
580 cell compartments of the tumor microenvironment. *Clin Cancer Res* 2010; 16:924-935.

581 [28] Hudson, H. M. and Larkin, R. S. Accelerated image reconstruction using ordered subsets
582 of projection data. *IEEE Trans Med Imaging* 1994; 13: 601–609.

583 [29] Hanessian, S.; Moitessier, N.; Gauchet, C.; Viau, M. N-Aryl sulfonyl homocysteine
584 inhibitors of matrix metalloproteinases: further probing of the S1, S1' and S2' pockets. *J Med*
585 *Chem* 2001; 44:3066-3073.

586 [30] Peng, Z.; Maxwell, D. S.; Sun, D.; Bhanu Prasad, B. A.; Pal, A.; Wang, S.; Balatoni, J.;
587 Ghosh, P.; Lim, S. T.; Volgin, A.; Shavrin, A.; Alauddin, M. M.; Gelovani, J. G.; Bornmann,
588 W. G. Imatinib analogs as potential agents for PET imaging of Bcr-Abl and c-KIT expression
589 at a kinase level. *Bioorg Med Chem* 2014; 1:623-632.

590

591 **Table 1:** *In vivo* plasma metabolite analysis of [¹⁸F]BR351 at different time points post tracer
592 injection. Values are expressed as % of total radioactivity, mean ± S.D. (n = 3). ND = not
593 detected.

Time p.i. (min)	Retention time on HPLC		
	M1 2 min	M2 3.5 min	[¹⁸ F]BR351 7 min
5 min	42.08 ± 2.45%	6.53 ± 0.51%	48.34 ± 2.60%
15 min	67.24 ± 6.06%	9.40 ± 0.44%	20.28 ± 5.41%
30 min	75.75 ± 4.31%	ND	12.17 ± 2.86%
120 min	80.45 ± 3.24%	ND	6.95 ± 0.95%

594